Mobile evaporite enhances the cycle of physical–chemical erosion in badlands

Ci-Jian Yang[1, 2], Pei-Hao Chen[1], Erica D. Erlanger[2], Jens M. Turowski[2], Sen Xu[2], Tse-Yang Teng[3], Jiun-Chuan Lin[1], Jr-Chuang Huang[1]

1. Department of Geography, National Taiwan University, No. 1, Sec. 4, Roosevelt Rd., Taipei 10617, Taiwan.
2. German Research Centre for Geosciences (GFZ), Telegrafenberg 14473, Potsdam, Germany.
3. Sustain-vision Consulting Co. Ltd., Taipei 11168, Taiwan.

Correspondence to: Ci-Jian Yang (d03228001@ntu.edu.tw)

Abstract. Chemical weathering driven by physical erosion is a natural process that strongly affects chemical and solid matter budgets at the Earth's surface. However, the influence of extreme climatic erosion on chemical weathering dynamics is poorly understood. Badland landscapes formed in highly erodible substrates have the potential to respond to individual events on scales that are rapid enough for direct observation. Here, we assess the geochemical and grain-size composition of suspended sediment and riverine chemistry measurements collected from two catchments during the 2017 Nesat and Haitang typhoons in southwestern Taiwan. During the typhoons, the Na^+ concentration covaried with suspended sediment concentration, which we attributed to sodium-induced deflocculation. Evaporite weathering at peak rainfall is succeeded by peak silicate weathering at maximum discharge. Overall, our observations suggest that initial weathering of near-surface evaporite enhances the physical erosion of silicate rock during extreme rainfall events.

1. Introduction

Chemical weathering induced by physical erosion controls nutrient supply to ecosystems (Milligan and Morel, 2002), reflects dynamic surface processes (e.g., Calmels et. al., 2011; Clift et. al., 2014; Emberson et. al., 2016; Meyer et. al., 2017), and regulates the global carbon cycle and the evolution of Earth's long-term climate (Berner et al., 1983; Ram et al., 1992; Gaillardet et al., 1999). In most landscapes, physical erosion and chemical weathering operate on geological timescales that may be difficult to observe on human timescales (e.g., Maher et al., 2014). However, in many landscapes erosion dominantly occurs during stochastic events, such as storms (e.g., Hartshorn et al., 2002; Lee et al., 2020; Wang et al., 2021). In particular, typhoons are able to transport large volumes of water and dissolved solids within hours to days, allowing us to observe the interactions between physical erosion and chemical weathering in landscapes impacted by them. Nevertheless, observations of the interaction between extreme physical erosion and chemical weathering dynamics are limited (Meyer et. al., 2017). Furthermore, the lack of high-frequency stream water sampling leads to a fundamental difficulty in constraining the dynamic behavior between physical erosion and chemical weathering during a high discharge period (e.g., a typhoon), which could have key implications for our ability to quantify topographic responses to these events.

Badlands are landscapes characterized by highly erodible and weathered substrates, that are largely devoid of vegetation. The high erodibility of these landscapes provides a unique opportunity to investigate and quantify denudation processes that operate at short timescales (Cheng et al., 2019; Yang et al, 2019, 2021a; 2021b). Badlands is typically dominated by mudstones and clays, and soils that contain clays saturated in sodium ions are particularly vulnerable to erosion by water. Sodium ions alter the layer charge of double-layered clay minerals (i.e. smectite) and cause the clays to deflocculate, which refers to the process of breaking up the clay (and ultimately the soil) into finer particles that are more easily washed away by water (e.g., Faulkner et al., 2004; Mitchell et al., 1993; Rengasamy and Olsson, 1991; Rengasamy et al.,1984; Sherard et al., 1976; Kašanin-Grubin et. al., 2018). Additionally,

mineral assemblage affects the stability of soil aggregates; for example, small amounts of smectite in kaolinitic materials cause it to be more dispersive and unstable (Levy et al., 1993).

Previous studies in the badlands of southwestern (SW) Taiwan have revealed that halite and gypsum dissolve at depth and migrate to the hillslope surface and deposit in desiccation cracks during the dry season (Higuchi et al., 2013, 2015; Nakata and Chigira, 2009). Others have observed that pore waters found in the near-surface mudstone have Na^+ concentrations of 1–3 million μmol/L at 1–2 cm depth (Nakata and Chigira, 2009). Mud cracks lead to the properties of the mudstone, e.g., rock density, water permeability, and ion concentration between the surface (a few centimeters to 10 cm depth) and bedrock are different (Fig. S1). For example, the bedrock hardly participates in physical erosion during a rainfall event due to low permeability. We hypothesize that the dissolved halite and gypsum re-crystallize in the near-surface and are deposited in the mudstone cracks through capillary action during the dry season. Subsequent precipitation dissolves the evaporite, and the dissolved Na^+ enhances erosion by clay dispersity and exposes more weatherable materials, forming a positive feedback cycle. Assuming a mudstone substrate that is primarily comprised of silicate minerals, we expect that concentration of evaporite ions should be consistent with changes in the sediment concentration and the concentration of silicate ions.

To investigate this potential feedback between evaporite dissolution and erosion, we use suspended sediment concentrations (SSC) and stream chemistry data from two catchments in the badlands of SW Taiwan (Fig. 1), collected at a temporal resolution of 3 hours over 3 days. We interpret our observations in the badlands to reflect how the excess sodium that re-precipitates at surface in dry season enhances physical erosion and chemical weathering in the following typhoon event.

2. Geological and Meteorological Setting

In Taiwan's badlands, the annual precipitation is about 2 m, and 90% of the rainfall is concentrated in the rainy season. The rainy season lasts from May to October and reaches its peak in August, with over 400 mm of precipitation within a single month. In contrast, less than 40 mm of average monthly rainfall is measured from November to April. We collected river water samples from two sites downstream of the studied badland areas. The first site, Nanxiong Bridge (NX), is located at the midstream of the Erren River and has a drainage area of 175 km^2. This area includes badlands covering an area of 4.37 km^2, which accounts for 2.49% of the total catchment area (Fig.1). The Erren River catchment is predominantly underlain by Plio-Pleistocene mudstones, which are several kilometers thick, and mainly feature illite (30.54%) and chlorite (28.70%) minerals (Tsai, 1984a). During the dry seasons, the pore water chemistry in the near-surface mudstones is mainly composed of Na^+, Cl^-, Ca^{2+} and SO_4^{2-} (Nakata and Chigira, 2009).

The gauging station at Nanxiong Bridge (NX) provides hourly discharge data for calculating sediment and solute fluxes. The annual average discharge of Nanxiong Bridge station is 10.2 m^3/s, and the typhoon season accounts for 84% of the total discharge. The meteorological station at Gutingkeng (GTK) is located 5.5 km from Nanxiong Bridge and provides hourly precipitation data. Our second sampling site is Guting (GT) Bridge, with an upstream drainage area of 79 km^2 and a badlands area of 1.87 km^2, corresponding to 2.37% of the total area. Guting Bridge is located adjacent to a badlands conservation area, so the riverine water chemistry reflects the weathering products derived from the adjacent hillslopes. Due to a lack of stream discharge observations at Guting Bridge, we use hourly precipitation data at GTK, which is less than 1 km from the sampling site, to quantify the impact of the typhoon events.
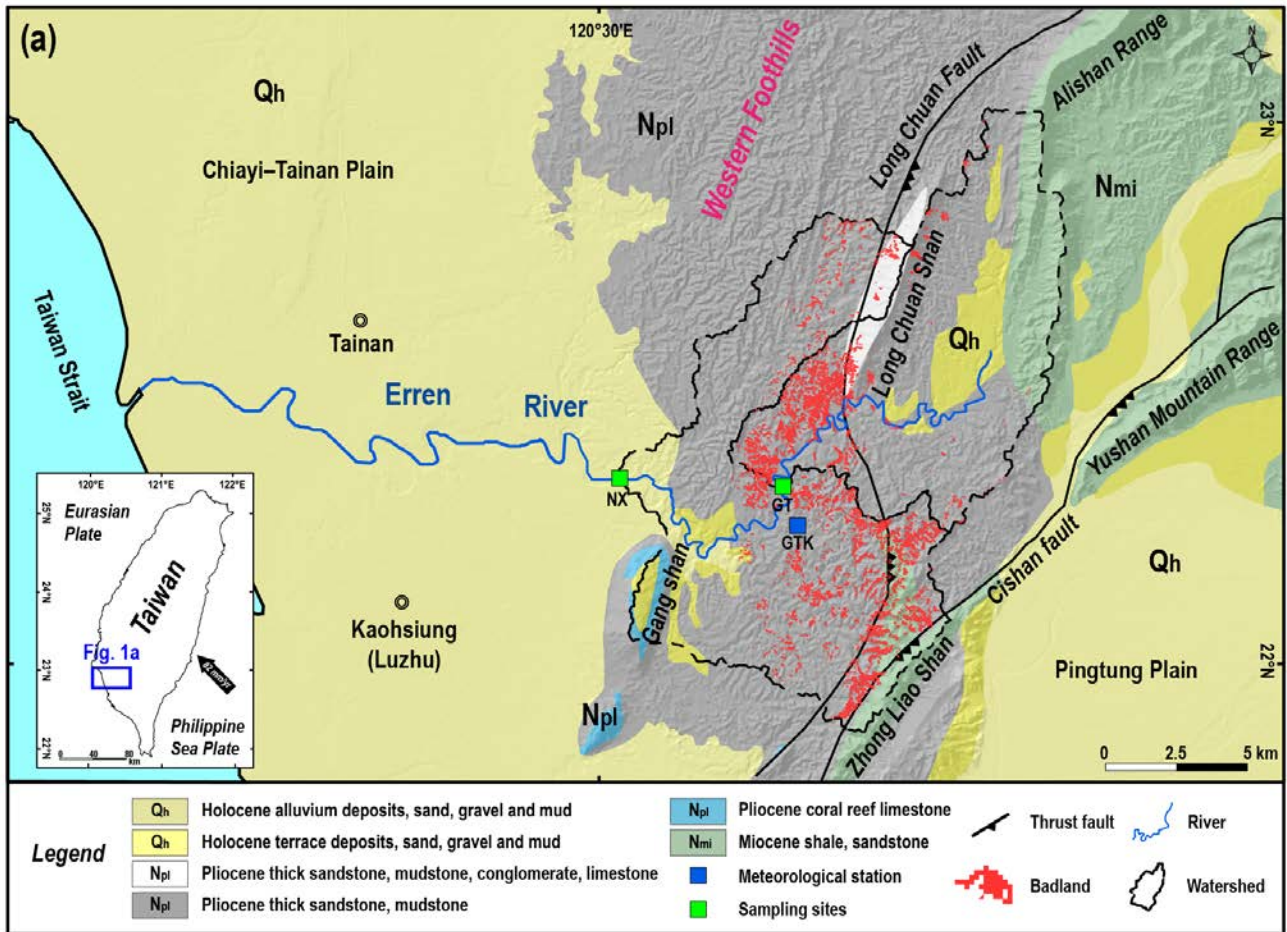
Figure 1. Location of sampling sites and geology of the study area. (a) The geological map of the study area (Source: Central Geological Survey, 2013). The green squares are sampling sites; hourly stream discharge data were obtained from the Nanxiong Bridge (NX) hydrometric station (Water Resources Agency). The blue square is the meteorological station, which provides hourly precipitation data (Central Weather Bureau, https://dbar.pccu.edu.tw/).

3. Methods and Materials

3.1 Water Sampling

We collected 42 stream samples from the two sampling sites for the typhoon period of July 2017. During sample collection, two 1000 ml PE bottles were dropped 1 to 2 meters below the water surface of the river simultaneously. Suspended sediment concentration (SSC) was subsequently calculated from the water collected in one of the PE bottles, and riverine chemistry was determined from water collected in the other bottle. Samples were filtered *in situ,* and the filtrate was preserved in the refrigerator for laboratory analysis. Additionally, 31 samples were collected from September 2014 to

110 December 2016 in the second half of every month at Nanxiong Bridge for non-typhoon periods, using

111 the same sampling procedure.

112

113 3.2 Dissolved load and sediment chemistry analysis

114 For the riverine dissolved load, we measured major dissolved anions (Cl^-, SO_4^{2-}, NO^{2-}, NO^{3-}, F^-) on an

115 Ion chromatography (IC, Metrohm Basic-883 plus), and we measured major dissolved cations (Na^+,

116 K^+, Mg^{2+}, Sr^{2+}, Ba^{2+}, Si^{4+}) on an ICP-OES (PerkinElmer, Optima 2100DV). We measured bulk

117 sediment chemistry from two samples of suspended sediment collected from Guting Bridge at low

118 flow before the typhoon event (2.26 m^3/s) and at the peak of runoff (724.32 m^3/s). About 0.7 g of dried

119 sediment sample was combusted in the muffle furnace at 650°C for 2 hours and then weighed to obtain

120 the loss on ignition (LOI). Afterward, an aliquot of ~100 mg from the residue was digested with a

121 mixture of concentrated HF and aqua regia. After digestion and drying, the sample was dissolved in

122 0.3 N HNO_3 for elemental determination. Major elemental concentrations of sediment samples were

123 obtained by ICP-OES (Varian 720-ES) at the GFZ German Research Centre for Geosciences.

124

125 **3.3 Grain size of suspended load**

126 Before measuring grain size, we removed the non-clastic deposition, i.e., sea salt, organic matter, and

127 carbonate. To remove sea salt, ~1 g of dried sediment sample was added to 15 ml of distilled water,

128 placed in a shaker, and shaken at a speed of 4000 rpm for 5 minutes. The centrifuged supernatant was

129 then poured out and these steps were repeated 3 times. To remove organic matter, 10 ml of a 15%

130 H_2O_2 solution was added to the sediment and placed in an ultrasonic oscillator for 24 hours. After

131 adding a second 10 ml of H_2O_2 (15%) to confirm the completion of the reaction, the mixture was

132 centrifuged and the supernatant containing the organic matter was removed. The sediment was then

133 washed by adding 30 ml of distilled water, and the supernatant was again removed after centrifugation.

134 This washing step was repeated 3 times to remove residual H_2O_2 in the centrifuge tube. To remove the

carbonates, we added 10 ml of 10% HCl solution to the centrifuge tube and allowed the acid to react

with the sediments for 24 hours. An additional 10 ml of HCl was then added to confirm the

completeness of the reaction. The sample was then centrifuged, and the supernatant was decanted to

remove the carbonates. The sample was then rinsed with 30 ml of distilled water, centrifuged, and

decanted. This step was performed 3 times to remove any residual HCl.

To disperse sediment agglomeration, we added 10 ml of 1% $Na(PO_3)_6$ solution to the sediment and let

the sample react for more than half a day. The grain size of the sediment samples was obtained by

Laser Diffraction Particle Size Analyzer LA950 at the GFZ German Research Centre for Geosciences.

By using LA950, we measured grains in the size range of between 100 nm to about 3 cm.

3.4 Calculation of the enriched ratio and sodium adsorption ratio (SAR)

In order to classify the supply of different ion sources during the typhoon event, we used the enriched

ratio of concentration as a reference. The enriched ratio is the ion concentration at a certain time

divided by the ion concentration at the first observation. A value greater than 1 represents a point in

time when the sample is more concentrated relative to the first observation, whereas a value smaller

than 1 represents a point in time when the sample is more diluted relative to the first observation. The

first observation was sampled 6 hours before the typhoon which represents the background value of

river water chemistry in this study.

Dissolved calcium and magnesium can stabilize soil aggregates and therefore enhance water

permeability (Nadler et al., 1996). By contrast, excess sodium can disperse soil particles through

deflocculation, thereby reducing water permeability (Hanson et al., 1999). The potential for material

dispersion in badlands is generally determined by measuring the presence and behavior of sodium and

is quantified by the sodium absorption ratio (SAR), (1):

160 $$SAR = \frac{Na^+}{\sqrt{\left(\frac{Ca^{2+}+Mg^{2+}}{2}\right)}} \tag{1}$$

161 Here, the cation measurements are expressed in milliequivalents per liter (meq/L). For pore water,

162 when SAR is greater than 13, the excess sodium causes soil particles to repel each other, preventing

163 the formation of soil aggregates (Seelig, 2000; Horneck et al., 2007). Given the influence of soil

164 structure, SAR value for irrigation water smaller than 3 is low, from 3 to 9 is medium and above 9 is

165 high (Ayers and Westcot, 1985).

166

167 3.5 Calculation of TDS and chemical weathering rate

168 Riverine TDS is widely used to estimate chemical weathering rates of river catchments (e.g. Gaillardet

169 et al. 1999). In this study, riverine TDS (in units of μmol/L) is expressed as:

170 $TDS = TDS_{rain} + TDS_{evaporite} + TDS_{sil} + TDS_{carb}$ (2)

171 where the contributions from precipitation (TDS_{rain}), evaporite ($TDS_{evaporite}$), silicate weathering

172 (TDS_{sil}) and carbonate weathering (TDS_{carb}) are considered. We calculated the proportions of ion

173 contributions from rainwater, evaporite, silicate and carbonate for Ca, Mg, Na, Cl, and SO_4 with the

174 MEANDIR inversion model (Kemeny and Torres, 2021), a MATLAB script for inverting fractional

175 contributions of end-members, and for constraining the chemical compositions of those end-members

176 with Monte Carlo propagation of uncertainty. To exclude the input of precipitation (TDS_{rain}) from

177 riverine TDS, we used local rainwater Cl^- concentrations with an average value of 68 μmol/L (Lu,

178 2014), and also the ratios of SO_4/Cl, Na/Cl, K/Cl, Mg/Cl, Ca/Cl in rainfall based on the rainfall

179 chemistry from 2007 to 2013 reported by Lu (2014) (Table 1).

180 $[X]_{norain} = [X]_{river} - [X]_{rain}$ (3)

181 $TDS_{rain} = \sum[X]_{rain}$ (4)

182 Here $[X]_{norain}$ reflects the remaining concentration of ion X after the removal of atmospheric inputs;

183 $[X]_{river}$ is the concentration of ion X in river water, and $[X]_{rain}$ is the concentration of ion X from

184 atmospheric deposition. In the second step, we corrected for evaporite inputs ($TDS_{evaporite}$) using the

185 following equation:

$$[X]_{NSS} = [X]_{norain} - [X]_{evap} = [X]_{norain} - \left([Cl]_{norain} \times \left(\frac{X}{Cl}\right)_{evap}\right) \tag{5}$$

$$TDS_{evaporite} = \sum[X]_{evap} \tag{6}$$

188 where $[X]_{NSS}$ is the concentration of ion X after the removal of ions attributed to evaporites, $[X]_{evap}$.

189 $[X/Cl]_{evap}$ is the ratio of ion X and Cl by using the end-member molar ratios of evaporite reported by

190 Burke et al. (2018), of which K/Cl is referred to Chao et al., (2011) (Table 1)). Then, after the correction

191 for evaporite, the chemical weathering budget can be divided into contributions by silicate (TDS_{sil})

192 and carbonate weathering (TDS_{carb}), expressed as:

$$TDS_{sil} = [Na]_{sil} + [K]_{sil} + [Mg]_{sil} + [Ca]_{sil} + [SiO_2]_{sil} \tag{7}$$

$$TDS_{carb} = [Mg]_{carb} + [Ca]_{carb} + [HCO_3]_{carb} \tag{8}$$

$$[HCO_3]_{carb} = \frac{1}{2}([Mg]_{carb} + [Ca]_{carb}) \tag{9}$$

196 where $[Na]_{sil}$ and $[K]_{sil}$ are riverine $[Na]_{NSS}$ and $[K]_{NSS}$ concentrations, respectively. We used

197 endmember values for silicate- and carbonate-dominated rocks reported by Gaillardet et al. (1999)

198 (Table 1). We agree that the use of global endmembers leads to a larger range of estimations, but is

199 still appropriate in discussing trends in weathering rates.

200 Considering the hydrological response, we use flow weighted method to calculate the flux of solute

201 (Huang et al., 2012), expressed as:

$$Flux_{(rain, \ evap, \ sil, \ carb)} = \left. \left(m \times \frac{\sum_{i=1}^{n} TDS_{(rain, \ evap, \ sil, \ carb) \ i}}{\sum_{i=1}^{n} Q_i} \times Q_t\right) \middle/ \text{catchment area} \right. \tag{10}$$

203 where m is the conversion factor for a specific unit (ton/km^2/yr). Q_i is the hourly discharge

204 corresponding to sampling time. Q_t is total discharge during the year or during the typhoon.

206 **Table 1** Input end-members for the MEANDIR inversion model.

End-member	SO$_4$/Cl	Na/ Cl	K/ Cl	Mg/Cl	Ca/Cl
Precipitation	0.35	0.90	0.09	0.18	0.35
Evaporites	0.6±0.6	1.0±0	0.026	0.1±0.08	0.5±0.5
	Ca/Na	Mg/Na			
Silicates	0.35±0.25	0.24±0.2			
Carbonates	60±30	30±15			

207

3.6 Calculation of total loss of mobile elements

209 The non-dimensional mass transfer coefficient ($\tau_{j, i}$) is used to quantify the loss or accumulation of a

210 mobile element (Anderson et al., 2002). Notably, we use the suspended sediment before the typhoon

211 event as the reference, instead of parent materials.

212 $$\tau_{i,j} = \frac{C_{j,p} C_{i,b}}{C_{j,b} C_{i,p}} - 1 \times 100 \tag{11}$$

213 Here, the concentration of an immobile element, Ti (C_i) or of a mobile element (C_j) in suspended

214 sediment is denoted for the time before peak discharge ($C_{i,b}$) or at peak discharge ($C_{i,p}$). When the τ

215 values approach -100, it indicates depletion, while values close to 100 indicate accumulation.

216

4. Results

4.1 Geochemistry of river water and suspended sediment

219 In 2017, the Nesat and Haitang typhoons brought 579 mm of rainfall over three days, with a maximum

220 intensity of 74 mm/hr. The discharge at Nanxiong Bridge demonstrated that the climatic co-response

221 has two pulses (Fig. 2). Since the time interval between the two typhoons was less than 6 hours, we

222 define the two typhoons as one typhoon event and distinguish between a first and second discharge

223 pulse. We quantify time relative to the onset of the typhoon (0 hr). The first pulse occurred from 8.5 to

224 32.5 hr, with a mean water discharge of 66.2 m^3/s. The second pulse that occurred from 32.5 to 62.5

225 hr had a 5.5 times higher mean discharge of 369.2 m^3/s. The maximum discharge (753.2 m^3/s) was

226 observed during the second pulse at 44.5 hr (July 31st, 2017, at 6:00 a.m.) (Fig. 2).

227

228 At Nanxiong Bridge, SSC has a statistically significant positive correlation with SAR ($\rho = 0.51$, $p <$

229 0.05). SSC has two peaks, one during each pulse, but SAR only shows a peak during the first pulse.

230 During the first pulse, SSC ranged from 10 to 33757 mg/L and SAR increased from 1.44 and to 3.14.

231 During the second pulse, SSC increased from 5445 to 16900 mg/L and SAR remained about 1.44.

232 The median grain size (D_{50}) ranged from 3.9 to 8.2 μm, with an average value of 5.6 μm during the

233 second pulse, and exhibited a positive correlation with discharge ($\rho = 0.40$). At Guting Bridge, SSC

234 has a statistically significant positive correlation with SAR ($\rho = 0.69$, $p < 0.05$) during the survey. SSC

235 ranged from 164 to 19538 mg/L before the first pulse and ranged from 2857 to 35920 mg/L during the

236 second pulse, while SAR showed a mean of 1.46 and two peaks with a value over 4 during both pulses.

237 D_{50} ranged from 3.6 to 8.8 μm, with an average value of 5.3 μm during the second pulse, (Fig. 2). In

238 terms of sediment chemistry at Guting Bridge, major elements of the two selected sediment samples

239 show that calcium and sodium accounted for about 10% of the mass loss between the typhoon event

240 (5.5 hr of duration) and the peak of discharge (41.5 hr of duration) (Table. S4).
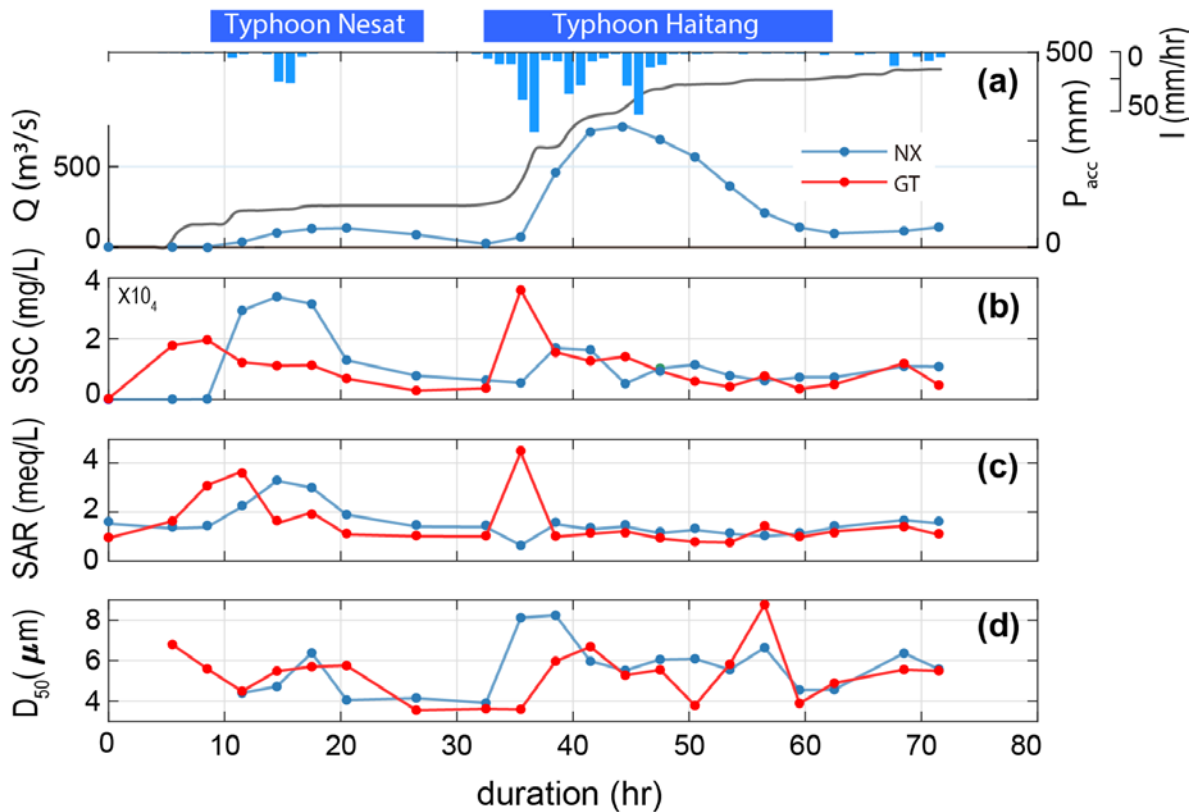
241

242 **Figure 2.** Timeseries SSC, SAR and median grain size of suspended sediment (D_{50}) at two sampling
243 sites. The blue line denotes hourly discharge (Q) at Nanxiong Bridge, and the blue bar denotes hourly
244 precipitation (I) at Gutingkeng station. The gray line denotes precipitation accumulation (P_{acc}), the blue
245 line denotes the Nanxiong Bridge (NX) dataset, and the red line denotes the Guting Bridge (GT) dataset.

246

247 The fractional proportions of TDS at Nanxiong Bridge during baseflow show that precipitation,

248 evaporites, silicates, and carbonates contribute 3.0±1.1% (uncertainty gives the standard error of the

249 mean), 28.7±14.6%, 26.9±6.5%, and 41.4±13.2%, respectively (Fig. 3a). During the typhoon event,

250 the proportion of TDS at Nanxiong Bridge attributed to TDS_{rain} is 6.3±2.4%. $TDS_{evaporite}$ contributes

251 32.4±13.6% and increases from 27.4% to 61.1% at the incipient first pulse. TDS_{sil} contributes

252 39.5±15.2%, which is 12.6% higher than the non-typhoon period. TDS_{carb} contributes 21.8±11.5 %

253 (Fig. 3b), which is 19.6% lower than the non-typhoon period. The fractional proportions of TDS at the

254 Guting Bridge show that 6.5±2.1% of TDS is contributed by TDS_{rain}. $TDS_{evaporite}$ contributes

255 24.8±16.2% and increases from 13.6% to 61.6% at the incipient second pulse, when the SSC and SAR

256 peak simultaneously. TDS_{sil} and TDS_{carb} contribute 39.5±15.2% and 27.5±16.7%, respectively (Fig.

257 3c).

258

259 Enriched ratios of less than one indicate dilution, and values greater than one indicate concentration.

260 Since we set the ion concentration of rainfall to be constant during the typhoon event, the enriched

261 ratio of precipitation is constant throughout the observation period. At Nanxiong Bridge, the evaporites

262 enriched ratio increases from 0.4 to 1.7 between the two pulses and decreases to 0.1 at the discharge

263 peak. The silicates enriched ratio increases from 1 to 1.5 before the first pulse and decreases to 0.1 at

264 the peak of discharge, then returns to 1 before the observation ends. The concentration attributed to

265 carbonates is always diluted. The evaporites and carbonates enriched ratio have a statistically

266 significant negative correlation with discharge (evaporites: ρ = -0.67, carbonates: -0.60, p<0.05) and

267 the silicate enriched ratio has a negative correlation with discharge (ρ = -0.32), indicating dilution by

268 typhoon rainfall (Fig. 3d). At Guting Bridge, the evaporites enriched ratio has two peaks during the

269 two pulses with a value of 5.2 at the first peak, a value of 4.7 at the second peak. After the event, the

270 value returns to about 1.2. Notably, the evaporites enriched ratios during both pulses are similar, but

271 the peak discharge of the second pulse is 5.5 times higher than that of the first pulse. The silicate

272   enriched ratio has an analogous pattern with the evaporites enriched ratio, but the enriched ratio is

273   smaller. Similar to Nanxiong Bridge, the carbonates enriched ratio is always diluted at Guting Bridge

274   (Fig. 3e). The evaporite and silicate enriched ratio shows a statistically significant positive correlation

275   ($\rho = 0.96$, p<0.05), and the evaporite and silicate enriched ratios have a statistically significant positive

276   correlation with SAR ($\rho = 0.86$, $\rho = 0.84$, p<0.05). We also use the concentration–discharge (cQ)

277   relationship of each ion at rising and recession limb, as well as baseflow at Nanxiong Bridge to assess

278   the state of dilution behavior (Fig. S2). Overall, our results show that all ions are in a dilution, and the

279   dilution in recession limb is stronger than that in rising limb, except for SO_4 during baseflow ($\theta=0.07$).

280   The concentration of Na, Cl and K during baseflow have a higher variability than the values during

281   the event. Additionally, Na, Cl, and SO_4 increase the concentration with increasing flow at the certain

282   period of rising limb.

283

284
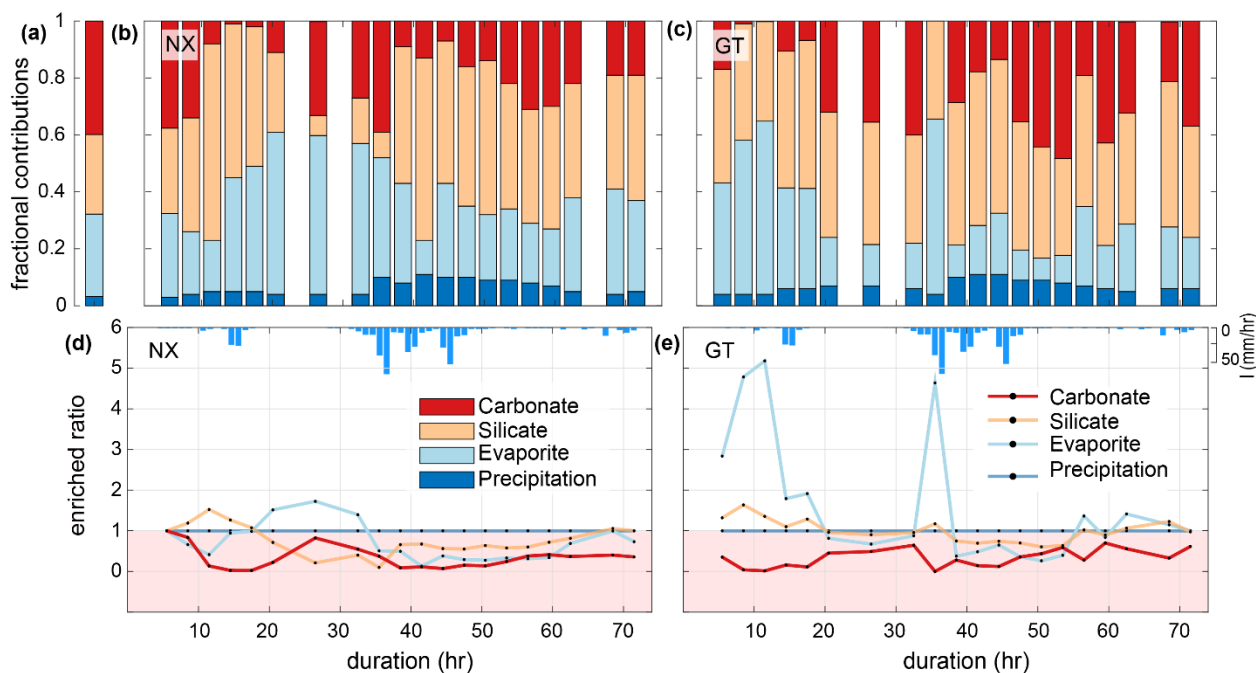
Figure 3. Timeseries illustrating TDS sources during the typhoon event at the two sampling sites. Fig.3a shows the average proportion of TDS for the non-typhoon period from September 2014 to December 2016 at Nanxiong Bridge; Fig.3b-c denotes the endmember contributions to TDS at Nanxiong Bridge dataset and Guting Bridge dataset from the typhoon period; the red bar denotes TDS_{carb} (Eq. 8); orange denotes TDS_{sil} (Eq. 7); the azure bar denotes $TDS_{evaporite}$ (Eq. 6); the blue bar denotes TDS_{rain} (Eq. 4). Fig.3d-e denotes the enriched ratio of ion concentrations by TDS sources from the Nanxiong Bridge dataset and Guting Bridge dataset during the typhoon period. The red line denotes TDS_{carb}, the orange line denotes TDS_{sil}, the azure line denotes $TDS_{evaporite}$, the blue line denotes the TDS_{rain}, and blue bar denotes hourly precipitation (I) at GTK station.

4.2 Evaporite, silicate and carbonate dissolution over time

We calculated the enriched ratios of ions (i.e., Na^+, Cl^-, Ca^{2+} and SO_4^{2-}) that are sourced from evaporites (i.e., halite (NaCl) and gypsum ($CaSO_4$)). The variability in the concentrations of each of these ions reflects the overall trends in TDS (Fig. 3d-e & Fig. 4).

At Nanxiong Bridge, all evaporite and carbonate ions have a statistically significant negative correlation with discharge. The enriched ratios in evaporite Na^+, Cl^- and SO_4^{2-} have the same trend (Fig. 4), which show an initial decrease during the first pulse, followed by an increase to 2 between the two pulses, and a final decrease during the second pulse. Evaporite Ca^{2+} shows a similar trend with evaporite Na^+, Cl^- and SO_4^{2-}, but the values are below 1. The enriched ratios of silicate Na^+, Ca^{2+} show an increase during the first pulse and a decrease to less than 1 before the rainfall peak, followed by an increase from about 0.06 to 1.11 at the end of observation. At Guting Bridge, all evaporite ions have a statistically significant positive correlation with the corresponding silicate ions (Na^+, $\rho = 0.98$; Ca^+, $\rho = 0.81$, $p < 0.05$). Evaporite Na^+, Cl^-, and SO_4^{2-} each have two peaks that occur prior to the maximum rainfall and reflect a factor of 5 increase in the enriched ratio. Compared with Nanxiong Bridge (downstream), the enriched ratio in evaporite Ca^{2+} at Guting Bridge concentrates at the onset of the first pulse and after peak discharge. Additionally, the enriched ratios of carbonate at Guting Bridge are similar to Nanxiong Bridge, and are always below 1.

312
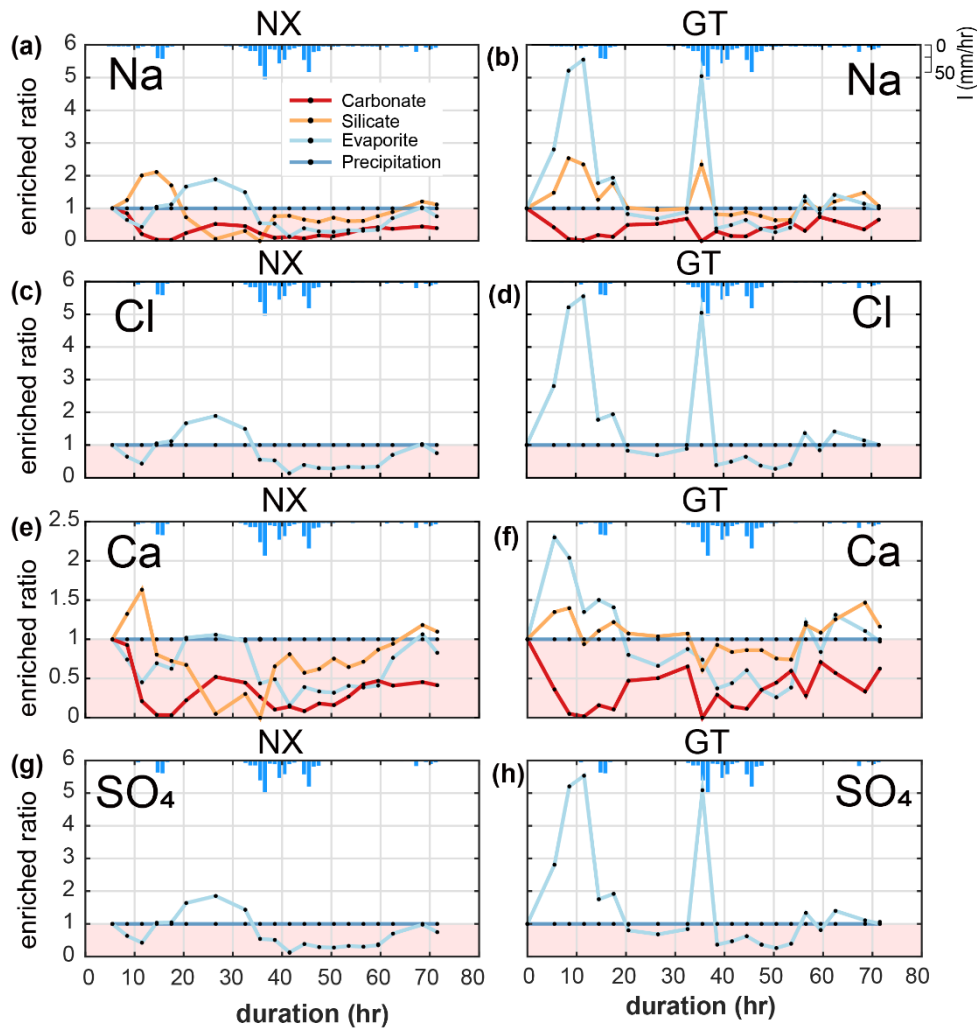
Figure 4. Time-series patterns in enriched ratio at two sampling sites. NX denotes the Nanxiong Bridge
dataset and GT denotes Guting Bridge dataset. The pink area indicates enriched values below 1. Blue
bar denotes hourly precipitation (I) at Gutingkeng station.

Gaillardet et al. (1999) documented that dissolved ions ratios of Ca/Sr and Na/Sr are distinct for

carbonates (low Na/Sr, high Ca/Na) versus silicates or evaporites (high Na/Sr, low Ca/Na). We use

these ratios to elucidate potential mixing between carbonates, silicates, and evaporite endmembers (Fig.

5). At Nanxiong Bridge, non-typhoon ratios of Na/(1000*Sr) and Ca/(1000*Sr) are 0.23–0.68 and

0.19–0.35, respectively (Table S4). These values increase markedly during the typhoon events, with

enriched– ratios of Na^+ exceeding 5 at T = 11.5 and 35.5 hr. The high concentration of Na^+, Cl^- and

SO_4^{2-} (as illustrated in the enriched ratio) indicate that there is enhanced dissolution of evaporites at

the onset of the typhoon event, especially at Guting Bridge. Subsequently, the concentration of Na^+

325 decreased with sustained rainfall. Then, the ratios approach the silicates/carbonates weathering (high

326 Na/Sr, high Ca/Sr ratios) after the peak discharge.

327
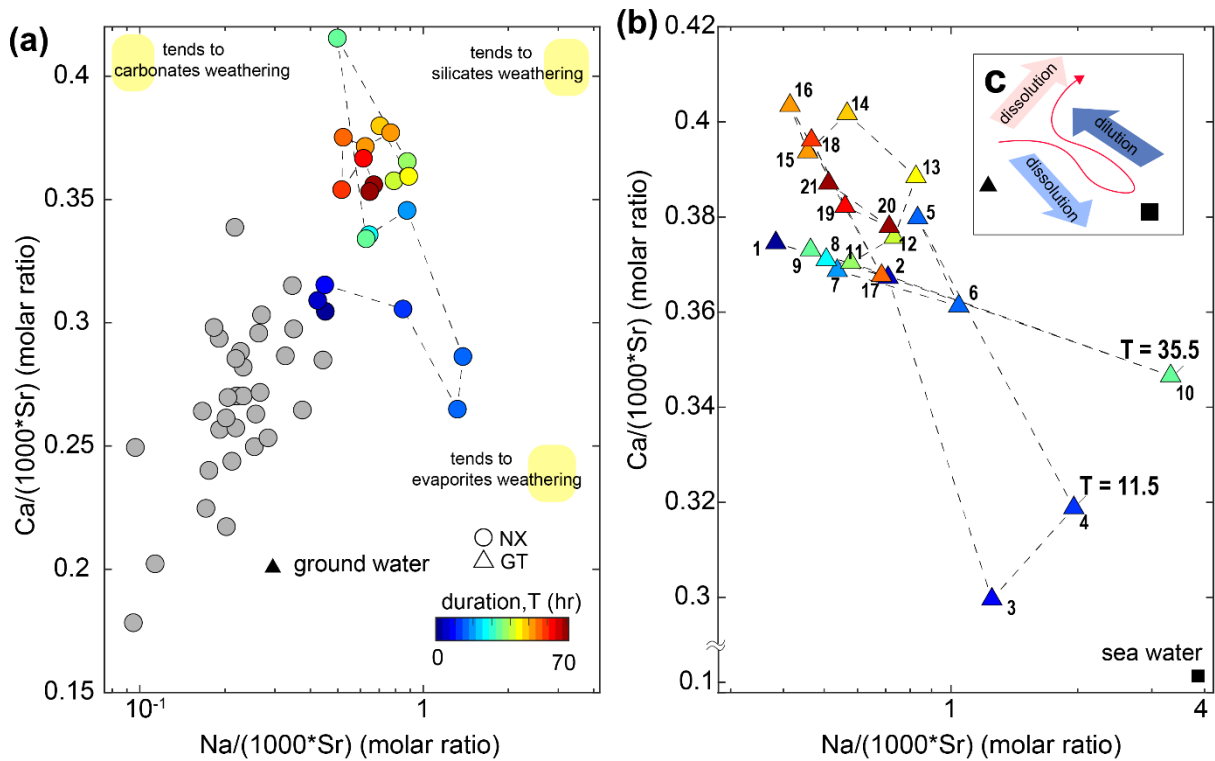
329 **Figure 5.** Molar ratio mixing diagrams of Erren River waters for (a-b) Na/(1000*Sr) versus

330 Ca/(1000*Sr), circles denote dataset at Nanxiong Bridge, and triangles denote dataset at Guting Bridge.

331 Colorbar denotes survey duration. Gray circles denote the dataset at Nanxiong Bridge during baseflow

332 conditions from 2014 to 2016. The black triangle illustrates the groundwater endmember (Chao et al.,

333 2011); the black square illustrates the seawater endmember. Numbers in the triangle represent the time

334 sequence, 1 represents the start point, and 21 represents the endpoint. Yellow areas indicate trends in

335 weathering types rather than the locations of endmember. (c) Illustration of dynamic weathering. The

336 red line indicates the direction of change with time. The light blue arrow denotes dissolution of

337 evaporite, the dark blue arrow denotes dilution from rainfall, and the red arrow denotes dissolution of

338 suspended sediment.

339

340 **5. Discussion**

341 **5.1 Relationships between dissolved evaporite and river water chemistry**

342 Before the survey, the monthly rainfall of the study area was 72.5 mm, which is only 18% of the

343 average monthly rainfall, implying that it provides a relatively dry environment for accumulating

344 evaporites on the slope surface. Under maximum rainfall intensity, Na^+, Cl^- and SO_4^{2+} at Guting Bridge

345 show markedly increased concentrations at the onset of the typhoon, peaks in enriched ratios that

346 exceed 5 (Fig. 4), and the greatest contribution of dissolved ions from evaporites (Fig. 3). Calculated

347 with pore water chemistry during the dry season from the same study site, the sodium absorptions ratio

348 (SAR) is 240.8 and exceeds the threshold value of 13. During the typhoon event, the river water SAR

349 has a maximum value of 4.41 at Guting Bridge (3.14 at Nanxiong Bridge), suggesting soil

350 deflocculation within river is weaker than on the hillslopes. However, the SAR has a statistically

351 significant positive correlation with $TDS_{evaporite}$ ($\rho = 0.86$, $p<0.05$) at Guting Bridge (upstream). This

352 pattern indicates that excess sodium is effective at inducing material dispersion at hillslopes and thus,

353 contributing to a higher suspended sediment load. The trend of river water SAR is able to reflect the

354 extent of dissolved Na^+ from hillslope. (Fig. 2).

355

356 These observations and results suggest that rainwater in the typhoon event rapidly dissolves the

357 evaporites on the slope surface, which produces high measured concentrations of Na^+, Cl^-, and SO_4^{2+}

358 during the time of peak precipitation (30-40 hr of duration). Furthermore, the dissolution of the near-

359 surface evaporite deposits should be most heavily influenced by runoff from the hillslopes, so we

360 expect that excess sodium and enhanced erosion will be most significant on the hillslopes.

361

362 At Nanxiong Bridge, we observe a 10-hour delay in the peak enriched ratio relative to the SAR (Fig.

363 3d) and overall lower enriched ratios relative to Guting Bridge (Fig. 3d-e). We suggest that dilution

364 and the transport distance from the badlands are responsible for this. The two catchments have a similar

365 areal extent of badlands within the total catchment area, which is about 2.49% at Nanxiong Bridge

366 catchment and 2.37 % in Guting Bridge catchment. Badlands contribute considerable evaporite solutes

367 (Chou, 2008), but the higher downstream drainage area will result in dilution of the solutes without

368 additional inputs. Additionally, Nakata and Chigira (2009) have observed that salt dissolution induces

369 an increase in electrical conductivity during intermittent rainfall events and decreases gradually after

370 rainfall events when evaporation and salt precipitate. Therefore, re-crystalization during the

371 transportation is to be expected.

372

373 **5.2 From evaporite dissolution to silicate weathering**

374 Our results show that the typhoon is responsible for mobilizing 16.8 ton/km^2/yr of dissolved solutes

375 derived from silicate weathering during the course of the event, and this flux corresponds to 16.6% of

376 the annual silicate weathering flux (Table S3). Additionally, we observed a change in the dominant

377 chemical weathering mechanism during the typhoon event. We rule out significant contributions from

378 baseflow and deep seawater after peak discharge, since ratios shift to higher Na/Sr, and Ca/Sr ratios

379 relative to the non-typhoon ratio (Fig. 5a–b), and the Ca/Sr ratio of mud volcanoes in the study site is

380 one order of magnitude less than river water (Chao et al., 2011). Carbonate weathering is the primary

381 contributor of Ca^{2+} for most of the world's large rivers (Gaillardet et al. 1999), but the increased Na$^+$

382 and consistently enriched ratio of carbonate Ca^{2+} does not make this a likely main contributor to the

383 Erren River during the typhoon. We thus suggest that the principal source of dissolved solutes is likely

384 to be silicate weathering.   This interpretation is supported by the temporal evolution of the enriched

385 ratio of silicate Ca^{2+}, which gradually increases after the discharge peak, to approach a value of about

386 1 at the end of survey (Fig. 4e&f). Therefore, we suggest that the ratios shift to higher Na/Sr, Ca/Sr

387 ratios due to enhanced silicate weathering during the typhoon. We also observe a 10–18% loss in the

388 individual concentrations of Ca, Na, Al, and Sr in the suspended sediment during the course of the

389 typhoon event, whereas concentrations of Fe, K, Mg, and Mn increase by 3-10% (Table S6). The

390 dissolution kinetics of silicate weathering are multiple orders of magnitude slower than carbonate or

391 evaporite weathering (Meybeck, 1987), suggesting that significant weathering of fresh silicate

392 minerals over the course of a single typhoon event is unlikely. Thus, the observed changes in ion

393 concentrations during the event are likely to arise from heterogeneities in the bedrock composition or

394   the input of previously weathered silicate minerals from a deeper groundwater reservoir (Calmels et

395   al., 2011), which is different from groundwater source of baseflow during non-typhoon period.

396   However, quantifying the role of a deeper groundwater inputs is difficult in the absence of isotope data.

397

398   Given that the sediment transported in the channel is supplied by physical erosion, we suggest that

399   physical erosion in our study site enhances silicate chemical weathering, which is consistent with

400   previous studies (Chung, 2002; Chou, 2008). Moreover, we associate the change in weathering regime

401   during the course of the typhoon with abrasive erosion of silicate sediments in the channel. Mechano-

402   chemical dissolution of weakly bound ions, e.g., F^- from the fresh muscovite surfaces is driven by

403   abrasion under high energy sediment transport with reorganization of the river bed (Andermann et al.,

404   2022). Mudstones are mainly composed of silicate minerals (e.g., illite and chlorite minerals) (Tsai,

405   1984a), and a few swelling clay minerals (e.g., montmorillonite), which provide an abundant silicate

406   pool. We suggest that high suspended sediment concentrations, combined with high energy flow during

407   the typhoon, caused increased silicate input from the weathered silicates in the suspended

408   sediment,which has also been observed in typhoon-driven silicate chemical weathering from silicate

409   minerals at surface (Meyer et. al., 2017). Importantly, the global annual silicate weathering flux of

410   rivers is 15.7 ton/km^2/yr (Gaillardet et al. 1999), relative to our value of 16.8 ton/km^2/yr., suggesting

411   that individual stochastic events may have global relevance.

412

413   **5.3 Typhoon-controlled cycles of physical and chemical erosion**

414   Evaporites, including halite (NaCl) and gypsum (CaSO$_4$), are found in few sedimentary environments,

415   and they are often excluded from the estimation of CO_2 consumption   (Gaillardet et al., 1999).

416   Compared to silicate rocks, the relation between evaporites weathering and physical erosion has rarely

417   been discussed. Through the interactions among riverine chemistry, suspended sediment properties,

418   and previous soil water chemistry studies, we suggest a positive feedback cycle of physical-chemical

419   erosion driven by mobile dissolved evaporite (Fig. 5). The feedback cycle includes three steps. (1)

420 precipitation and deposition of evaporite during the dry season in near-surface mudstone desiccation

421 cracks through capillary transport (Higuchi et al., 2013, 2015; Nakata and Chigira, 2009). In the dry

422 season, exposed bedrock with low water content develops desiccation cracks (Allen, 1982; Goehring

423 et al., 2010; Kindle, 1917; Seghir and Arscott, 2015; Xiaa and Hutchinson, 2000), providing space for

424 the re-precipitation of evaporite minerals. Using evidence from core samples in mudstone bedrock at

425 the study site, the depth of the crack of about 20 cm can be regarded as the thickness of the weathering

426 layer. Higuchi et al. (2013) suggested that the weathering layer in the top 10 cm of mudstone can easily

427 be eroded by intense rainfall. Erosion exposes fresh bedrock, which would dry in the following dry

428 season and further produce weatherable material.

429

430 (2) Rainfall dissolves the evaporites, producing sodic water that increases physical erosion during

431 typhoon events. The resulting dissolved sodium causes higher hillslope erosion by deflocculation,

432 leading to increased suspended sediment in the channels. In the study site, hillslope erosion rate is

433 about 9-30 cm/year (Higuchi et al., 2013; Yang et al., 2021a). At Nanxiong Bridge, the denudation rate

434 approaches about 142,857 ton/km^2/yr, measured from river suspended load (Dadson et. al., 2003), and

435 the chemical weathering flux is 124-237 ton/km^2/yr (Chou, 2008; this study). The high hillslope

436 erosion rate ensures a steady supply of freshly exposed bedrock, allowing for high chemical weathering

437 rates.

438

439 (3) Physical erosion enhances silicate weathering and bedrock exposure on hillslopes. Clay minerals

440 in mudstone deposits are abraded from the abundantly available sediment and provide material for

441 silicate weathering in streams. Ultimately, with frequent typhoon events and high temperatures in the

442 study area, this dynamic cycle could repeat several times a year.

443
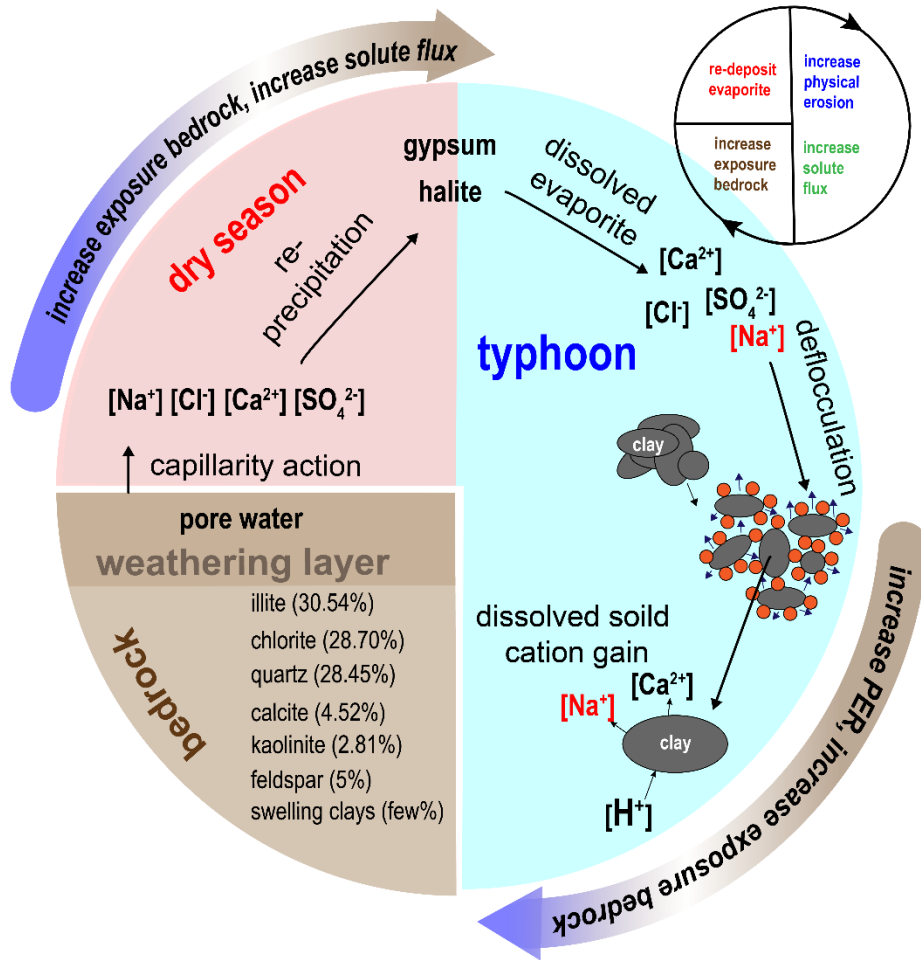
Figure. 6. Cycle of feedback between physical erosion rate (PER) and solute flux in badlands catchment. Red blocks represent dry season conditions. Blue region represents typhoon conditions. Brown region represents the bedrock and indicates the type and proportion of minerals of mudstone (Tsai, 1984b).

448

6. Conclusion

We presented major element compositions of stream water from two sites in the Erren River catchment at three-hour intervals during a three-day typhoon event in 2017. At Guting Station (upstream), $TDS_{evaporite}$ is covariant with TDS_{sil}, the sodium adsorption ratio, and the suspended sediment concentration, which can be assigned to dissolved evaporite (e.g., halite and gypsum). The excess sodium in the evaporite deposits causes material dispersion through deflocculation, which enhances the suspended sediment flux. Our observations show that the water chemistry of the typhoon event is mainly contributed by silicate weathering at 16.8 ton/km^2/yr and evaporite weathering at 10.9

ton/km^2/yr, in contrast with baseflow (non-typhoon) conditions that are mainly contributed by carbonate weathering. Moreover, during the course of the typhoon, we observed a shift from predominantly evaporite weathering during peak precipitation to silicate weathering at peak discharge.

Combining the observation of riverine chemistry, suspended sediment properties, and previous soil water chemistry studies, we propose a feedback cycle between physical erosion and chemical weathering in badlands topography, illustrating that precipitation of evaporites during the dry season produces sodic water during typhoon events and preferentially triggers higher local erosion. The enhanced hillslope erosion and abrasive effects of clay in a high discharge stream enhance bedrock exposure on hillslopes and silicate weathering, respectively. Newly exposed bedrock then produces more weathered material. Although measurements of bedrock mineral chemistry and Sr isotope are still needed for confirming sources of excess sodium and calcium (Fig. 5), we suggest that the conceptual model could provide an insight into landscape change of badlands. The results from our study suggest that high erosion rates in mudstone badlands of the Erren River catchment are due to both weakened lithology and the interaction between evaporites and hillslope erosion.

Data availability. Relevant data supporting the findings of the study are available in the Supplementary Information, or from the corresponding author upon request. Source data are provided with this paper.

Author contributions. C.-J.Y. designed the study and conducted field surveys, data analysis, and modeling. P.-H. C. conducted data analysis. S. X. conducted modeling. T. Y. T. provided the verified data. J.-C.L. and J.-C. Huang contributed to the scientific discussion and interpretation. C.-J.Y., E. D. E. and J.M.T. wrote the paper with the input of all authors.

Competing interests. The authors declare that they have no competing interests.

Acknowledgements. We express our gratitude to Kai Deng, Chao-Yuan Lin and Niels Hovius for fruitful discussions that greatly improved this work. Special thanks are also given to Sheng-Wei Guo, Meng-Chang Lu for field work, Kai Deng for sediment chemistry analysis, and David Puhl for assistance of grainsize analysis. This is study was supported by grants from National Science and Technology Council, Taiwan to Ci-Jian Yang (MOST 110-2917-I-564-009-).

References

1. Allen, J.R.L.: Sedimentary structures: Their Character and Physical Basis. Developments in sedimentology. 30B, II. Elsevier, Amsterdam. 1982.

2. Andermann, C., Galy, A., Hennig, S., Zimmermann, B., Tipper, E. T., Erlanger, E., Cook, K. L., Schleicher, A., Benning, L., and Hovius, N.: Erosion and weathering forensics of a catastrophic glacial lake outburst flood in Nepal, EGU General Assembly 2022, Vienna, Austria, 23–27 May 2022, EGU22-10417, https://doi.org/10.5194/egusphere-egu22-10417, 2022.

3. Anderson, S.P., Dietrich, W.E., Brimhall, G.H.: Weathering profiles, mass-balance analysis, and rates of solute loss: linkages between weathering and ero-sion in a small, steep catchment. Bull. Geol. Soc. Am.114, 1143–1158. https://doi .org /10 .1130 /0016 - 7606(2002)114<1143 :WPMBAA >2 .0 .CO, 2002.

4. Ayers, R., Westcot, D.: Water quality for agriculture. FAO Irrigation and drainage paper 29, 1985.

5. Burke, A., Present, T., Paris, G. Rae, Emily C.M., Sandilands, B. Gaillarde, J., Peucker-Ehrenbrink, B., Fischer, W. W., McClelland, J. W., Spencer, R. G. M., Voss, B. M., Adkins, J. F.: Sulfur isotopes in rivers: Insights into global weathering budgets, pyrite oxidation, and the modern sulfur cycle. Earth and Planetary Science Letters, 496. https://doi.org/10.1016/j.epsl.2018.05.022, 2018

6. Calmels, D., Galy, A., Hovius, N., Bickle, M. J., West, A. J., Chen, M.-C., Chapman, H.: Contribution of deep groundwater to the weathering budget in a rapidly eroding mountain belt, Taiwan. Earth and Planetary Science Letters, 303 (1-2), 48–58.

509   https://doi.org/10.1016/j.epsl.2010.12.032, 2011

510   7. Carey, A. E., Gardner, C. B., Goldsmith, S. T., Lyons, W. B., Hicks, D. M.: Organic carbon yields

511   from small, mountainous rivers, New Zealand. Geophysical Research Letters, 32, 15404.

512   https://doi.org/0.1029/2005GL023159, 2005.

513   8. Chao, H.-C., You, C.-F., Wang, B.-S., Chung, C.-H., Huang, K.-F.: Boron isotopic composition of

514   mud volcano fluids: Implications for fluid migration in shallow subduction zones. Earth and

515   Planetary Science Letters, 305. https://doi.org/10.1016/j.epsl.2011.02.033, 2011.

516   9. Cheng, Y.-C., Yang, C.-J., Lin, J.-C.: Application for Terrestrial LiDAR on Mudstone Erosion

517   Caused by Typhoons. Remote sensing, 11(20), 2425. https://doi.org/10.3390/rs11202425, 2019.

518 10. Chou, C.-L.: Sediment Weathering and River Water Chemistry in the Erren Drainage Basin,

519   Southern Taiwan. Master thesis of Department of Earth Sciences, National Cheng Kung

520   University, 1–103, 2008.

521 11. Chung, S.-L.: Preliminary Geochemical and Isotopes study of the Erren river water. Master thesis

522   of Department of Earth Sciences, National Cheng Kung University, 1–95, 2002.

523 12. Clift, P. D., Wan, S., Blusztajn, J.: Reconstructing chemical weathering, physical erosion and

524   monsoon intensity since 25Ma in the northern South China Sea: A review of competing proxies.

525   Earth-Science Reviews, 130, 86–102. https://doi.org/10.1016/j.earscirev.2014.01.002, 2014.

526 13. Dadson, S. J., Hovius, N., Chen, H., Dade, W. B., Hsieh, M.-L., Willett, S. D., Hu, J.-C., Horng,

527   M.-J., Chen, M.-C., Stark, C. P., Lague, D. Lin, J.-C.: Links between erosion, runoff variability

528   and seismicity in the Taiwan orogen. Nature, 426(6967), 648–651,

529   https://doi.org/10.1038/nature02150, 2003.

530 14. Emberson, R., Hovius, N., Galy, A., Marc, O.: Chemical weathering in active mountain belts

531   controlled by stochastic bedrock landsliding. Nature Geoscience, 9, 42–47.

532   https://doi.org/10.1038/ngeo2600, 2016.

533 15. Faulkner, H., Alexander, R., Teeuw, R., Zukowskyj, P.: Variations in soil dispersivity across a

534   gully head displaying shallow sub-surface pipes, and the role of shallow pipes in rill initiation.

535   Earth Surface Process and Landforms. 29, 1143–1160. https://doi.org/10.1002/esp.1109, 2004.

536   16. Gaillardet, J., Dupre, B., Louvat, P., Allegre, C. J.: Global silicate weathering and CO_2

537   consumption rates deduced from the chemistry of large rivers. Chemical Geology, 159, 3–30.

538   https://doi.org/10.1016/S0009-2541(99)00031-5, 1999.

539   17. Goehring, L., Conroy, R., Akhter, A., Cleggb, W.J., Routh, A.F.: Evolution of mud-crack patterns

540   during repeated drying cycles. Soft Matter, 6, 3562–3567. https://doi.org/10.1039/B922206E,

541   2010.

542   18. Hanson, B., Grattan, SR., Fulton, A.: Agricultural salinity and drainage. University of California

543   Irrigation Program, Davis., 1999.

544   19. Hartshorn, K., Hovius, N., Dade, W. B. Slingerland, R. L.: Climate-Driven Bedrock Incision in

545   an Active Mountain Belt. Science, 297, 2036–2038. https://10.1126/science.1075078, 2002.

546   20. Higuchi, K., Chigira, M., Lee, D.-H.: High rates of erosion and rapid weathering in a Plio-

547   Pleistocene mudstone badland, Taiwan. Catena, 106, 68–82.

548   https://doi.org/10.1016/j.catena.2012.11.005, 2013.

549   21. Higuchi, K., Chigira, M., Lee, D-H., Wu, J-H.: Rapid weathering and erosion of mudstone

550   induced by saltwater migration near a slope surface. Journal of Hydrologic Engineering, 20(6),

551   C6014004. https://doi.org/10.1061/(ASCE)HE.1943-5584.0001105, 2015.

552   22. Horneck, D.S., Ellsworth, J.W., Hopkins, B.G., Sullivan, D.M., Stevens, R.G.: Managing Salt-

553   Affected Soils for Crop Production. PNW 601-E. Oregon State University, University of Idaho,

554   Washington State University, 2007.

555   23. Huang, J.C., Lee, T.Y., Kao, S.J., Hsu, S.C., Lin, H.J., Peng, T.R.: Land use effect and

556   hydrological control on nitrate yield in subtropical mountainous watersheds. Hydrology and

557   Earth System Science, 16(3), 699-714. https://doi.org/10.5194/hess-16-699-2012, 2012.

558   24. Kemeny, P. C., Torres, M. A.: Presentation and applications of mixing elements and dissolved

559   isotopes in rivers (MEANDIR), a customizable MATLAB model for Monte Carlo inversion of

560   dissolved river chemistry. American Journal of Science, 321(5), 579–642.

561   https://doi.org/10.2475/05.2021.03, 2021.

562   25. Kindle, E.M.: Some factors affecting the development of mud-cracks. The Journal of Geology,

563   25(2), 135–144. https://doi.org/10.1086/622446, 1917.

564   26. Knapp, J. L., von Freyberg, J., Studer, B., Kiewiet, L., & Kirchner, J. W.: Concentration–

565   discharge relationships vary among hydrological events, reflecting differences in event

566   characteristics. Hydrology and Earth System Sciences, 24(5), 2561-2576.

567   https://doi.org/10.5194/hess-24-2561-2020, 2020.

568   27. Lee, D.-H., Lin, H.-M., Wu, J.-H.: The basic properties of mudstone slopes in southwestern

569   Taiwan. Journal of GeoEngineering, 2(3), 81–95. https://doi.org/10.6310/jog.2007.2(3).1, 2007.

570   28. Lee, Y.-J., Chen, P.-H., Lee, T.-Y., Shih, Y.-T., Huang, J.-C.: Temporal variation of chemical

571   weathering rate, source shifting and relationship with physical erosion in small mountainous

572   rivers, Taiwan, Catena, 190. https://doi.org/10.1016/j.catena.2020.104516, 2020.

573   29. Lu, S.-C. and Lin, N.-H.: Monitoring and component analysis of acid rain research

574   project. Environmental Protection Agency, Taiwan, 2014.

575   30. Lyons, W. B., Carey, A. E., Hicks, D. M., Nezat, C. A.: Chemical weathering in high-sediment-

576   yielding watersheds, New Zealand. Journal of Geophysical Research-Earth Surface, 110, 11.

577   https://doi.org/10.1029/2003JF000088, 2005.

578   31. Maher, K., and Chamberiain, C. P.: Hydrological Regulation of Chemical Weathering and the

579   Geologic Carbon Cycle. Science, 343, 1502–1504. https://doi.org/10.1126/science.1250770,

580   2014.

581   32. Meyer, K. J., Carey, A. E., You, C.-F.: Typhoon impacts on chemical weathering source

582   provenance of a High Standing Island watershed, Taiwan. Geochimica et Cosmochimica Acta,

583   215, 404–420. https://doi.org/10.1016/j.gca.2017.07.015, 2017.

584   33. Mitchell, J. K.: Volume change behavior. In: Mitchell, J.K., Soga, K. (Eds.), Fundamentals of

585   Soil Behavior. Wiley, 293–333, 1993.

586   34. Moon, S., Huh, Y., Qin, J.H., van Pho, N.: Chemical weathering in the Hong (Red) River basin:

587   Rates of silicate weathering and their controlling factors. Geochimica et Cosmochimica Acta, 71,

588   1411–1430. https://doi.org/10.1016/j.gca.2006.12.004, 2007.

589 35. Nadler, A., Levy, G. J., Keren, R., Eisenberg, H.: Sodic Calcareous Soil Reclamation as Affected

590   by Water Chemical Composition and Flow Rate. Soil Science Society of America Journal. 60 (1):

591   252. Bibcode:1996SSASJ.60.252N. https://doi:10.2136/sssaj1996.03615995006000010038x,

592   1996.

593 36. Nakata, E., Chigira, M.: Geochemistry of erosion processes on badland slopes. A case study of

594   the Gutingkeng formation where mud volcanoes are distributed in southern Taiwan. Journal of

595   Geography, 118(3), 511–532, 2009.

596 37. Negrel, P., Allegre, C.J., Dupre, B., Lewin, E.: Erosion sources determined by inversion of major

597   and trace element ratios and strontium isotopic ratios in river water: The Congo Basin case. Earth

598   and Planetary Science Letters, 120, 59–76. https://doi.org/10.1016/0012-821X(93)90023-3, 1993.

599 38. Rengasamy, P., Greene, R.S.B., Ford, G.W., Mehanni, A.H.: Identification of dispersive behavior

600   and the management of red-brown earths. Australian Journal of Soil Research, 22, 413–443.

601   https://doi.org/10.1071/SR9840413, 1984.

602 39. Rengasamy, P., Olsson, K. A.: Sodicity and soil structure. *Australian Journal of Soil Research*,

603   29, 935–952. https://doi.org/10.1071/SR9910935, 1991.

604 40. Seelig, B. D.: Salinity and Sodicity in North Dakota Soils. EB-57. North Dakota State University,

605   Fargo, ND, 2000.

606 41. Seghir, R., Arscott, S.: Controlled mud-crack patterning and self-organized cracking of

607   polydimeth. Scientific Report, 5, 14787. https://doi.org/10.1038/srep14787, 2015.

608 42. Sherard, J. L., Dunnigan, L. P., Decker, R. S., Steele, E. F.: Identification and nature of dispersive

609   soils. Journal of the Geotechnical Engineering Division, 102, 287–301. 1976.

610 43. Tsai, J. S.: The study on basic properties of mudstone and stabilization methods for   mudstone

611   cut slope in southwestern Taiwan. Master Thesis of Civil Engineering Department, National

612   Cheng Kung University, Tainan, Taiwan, 1984b.

613 44. Xia, Z. C., Hutchinson, J. W.: Crack patterns in thin flms. Journal of the Mechanics and Physics

614   of Solids, 48, 1107–1131. https://doi.org/10.1016/S0022-5096(99)00081-2, 2000.

615   45. Yang, C.-J., Turowski, J. M. Hovius, N., Lin, J.-C., Chang. K.-J.: Badland landscape response to

616   individual geomorphic events. Nature Communications, 12(1):4631.

617   https://doi.org/10.1038/s41467-021-24903-1, 2021a.

618   46. Yang, C.-J., Jen, C.-H., Cheng, Y.-C., Lin, J.-C.: Quantification of mudcracks-driven erosion

619   using terrestrial laser scanning in laboratory runoff experiment. Geomorphology, 375.

620   https://doi.org/10.1016/j.geomorph.2020.107527, 2021b.

621   47. Yang, C.-J., Yeh, L.-W., Cheng, Y.-C., Jen, C.-H., Lin, J.-C.: Badland Erosion and Its

622   Morphometric Features in the Tropical Monsoon Area. Remote sensing, 11(24), 3051.

623   https://doi.org/10.3390/rs11243051, 2019.